Journal of the Mechanics and Physics of Solids 95 (2016) 169–187

Contents lists available at ScienceDirect

Journal of the Mechanics and Physics of Solids

journal homepage: www.elsevier.com/locate/jmps

Multiscale coupling of molecular dynamics and peridynamics

Qi Tong, Shaofan Li *

Department of Civil and Environmental Engineering, University of California, Berkeley, CA 94720, USA

ARTICLE INFO

Article history:
Received 16 December 2015
Received in revised form
15 May 2016
Accepted 29 May 2016
Available online 4 June 2016

Keywords:
Fracture
Molecular dynamics
Multiscale coupling
Peridynamics
Solid mechanics

ABSTRACT

We propose a multiscale computational model to couple molecular dynamics and peridynamics. The multiscale coupling model is based on a previously developed multiscale micromorphic molecular dynamics (MMMD) theory, which has three dynamics equations at three different scales, namely, microscale, mesoscale, and macroscale. In the proposed multiscale coupling approach, we divide the simulation domain into atomistic region and macroscale region. Molecular dynamics is used to simulate atom motions in atomistic region, and peridynamics is used to simulate macroscale material point motions in macroscale region, and both methods are nonlocal particle methods. A transition zone is introduced as a messenger to pass the information between the two regions or scales. We employ the "supercell" developed in the MMMD theory as the transition element, which is named as the adaptive multiscale element due to its ability of passing information from different scales, because the adaptive multiscale element can realize both top-down and bottom-up communications. We introduce the Cauchy–Born rule based stress evaluation into state-based peridynamics formulation to formulate atomistic-enriched constitutive relations. To mitigate the issue of wave reflection on the interface, a filter is constructed by switching on and off the MMMD dynamic equations at different scales. Benchmark tests of one-dimensional (1-D) and two-dimensional (2-D) wave propagations from atomistic region to macro region are presented. The mechanical wave can transit through the interface smoothly without spurious wave deflections, and the filtering process is proven to be efficient.

1. Introduction

Computer technology has been transforming scientific and engineering researches. The ever powerful computer and advanced computational algorithms open up opportunities to help us model materials in great details and in unprecedented precisions. For example, the state-of-the-art computational theory and technology, such as ab initio computations and molecular dynamics, e.g. Hohenberg and Kohn (1964), Car and Parrinello (1985), Kohn and Sham (1965), enable us to simulate and predict motions of electrons and atoms with indomitable resolution. Compared with experimental study, computer simulation is fast, cheaper, more efficient, and both informative and flexible, which greatly expands the frontier of researches in many disciplines including materials science, biology, chemistry, etc. The state-of-the-art exascale supercomputer is now capable of handling a molecular system up to sub-millimeter with 110 billion (1.1×10^{11}) atoms (Hou et al., 2012). However, the simulation of a molecular system of macroscale size with 6.022×10^{23} atoms and above is still out of

* Corresponding author.
E-mail address: shaofan@berkeley.edu (S. Li).

http://dx.doi.org/10.1016/j.jmps.2016.05.032
0022-5096/

reach by even the largest and the faster computers, not to mention the common purpose computers. First principle calculation is even more limited in spatial and time scales because of the calculation of electronic structures. Another challenge is how to analyze and extract useful information from large amount of data that is generated from computer simulations. In engineering research and developments, phenomenological models based finite element analysis and finite difference analysis provide useful tools of simulating continuum objects at macroscopic scale. By virtue of interpolation and discretization of continuum fields, requirements on computer capacity are greatly alleviated. However, macroscale material models usually employ homogenized field variables and adopt empirical assumptions, such as phenomenological constitutive relations, in which some detailed physical information may be lost, making it difficult to understand multiscale physical behaviors of materials, for instance, microscale and mesoscale material defect evolutions.

The limitation of computational model in each scale has motivated the development of various multiscale simulations, concurrent or hierarchical. The goal of a multiscale model is to combine physical theories or mathematical models from different scales in a single framework, so that we can solve the multiscale problem in either a distinctive scale or simultaneously concurrent scales depending on the problems of interest. The possibility of scale division is based on two factors. First, physical nature of materials manifests itself in multiple scales in space and time. Materials defects and flaws are typical multiscale phenomena. For example, microscopic dislocation largely determines the macroscale strength of the material; highly localized region around the crack tip that is characterized by bond breaking and strong discontinuity, but the region where is away from the crack tip may only have moderate or uniform deformation. Second, reliable coupling techniques are required to transfer information among different scales. Cross-scale communication is one of the most challenging issues in both multiscale theory and computer simulations, because quantities in different scales have distinct properties, and a perfect match between them is often difficult. For examples, force in microscale may be described in terms of nonlocal interaction between two or many particles interaction, whereas in macroscale it is often described in terms of local interaction among immediate adjacent particles; and temperature is a concept in macroscale, and its corresponding microscale phenomenon is the random motion of particles.

Several multiscale models have had some success in practice. Among them, the macroscopic, atomistic, ab initio dynamics (MAAD) (Abraham et al., 1998; Broughton et al., 1999) method is one of the earlier works, which spans three scales from quantum mechanics to continuum mechanics. It has been applied to solve dynamical fracture problem of silicon. On the other hand, the issue of numerical wave reflection at interscale boundary can be observed in this method. The quasi-continuum method (Tadmor et al., 1996; Shenoy et al., 1998, 1999; Knap and Ortiz, 2001) is another widely recognized model, in which only representative atoms are being simulated instead of conducting all atom calculations, and it has been successful in solving some quasi-static problems such as nano indentation.

However, MAAD method has interscale boundary impedance mismatch problem, and the quasi-continuum method is restricted to static and quasi-static problems without characterization of dynamics. Moreover, the mismatch of the impedance at the inter-scale boundary forces to introduce a so-called “ghost force”. To resolve the inter-scale boundary mismatch problem, the bridging scale method (Wagner and Liu, 2003; Park et al., 2005a, 2005b; Liu et al., 2006) provides a procedure that can realize the scale transition by a process of projection with minimizing least square error, and it introduces an impedance force that may largely alleviated the inter-scale boundary wave reflection. The coupled atomistic and discrete dislocation (CADD) (Shilkrot et al., 2002, 2004) is advantageous to simulate dislocation-type of defects, and it may involve a priori knowledge of slip systems for dislocation detection and passing through interfaces. The recently proposed Multiscale Crystal Defect Dynamics (MCDD) (Li et al., 2014) employs a similar idea by using information of the lattice microstructure to construct multiscale methods. Other prominent multiscale methods include concurrent atomistic continuum (CAC) method (Chen and Lee, 2005; Xiong et al., 2011), and the perfectly matched multiscale simulation (PMMS) method (To and Li, 2005; Li et al., 2006), among others.

Theoretically speaking, an ideal multiscale method would need to have a two-way cross-scale information passage: the bottom-up and the top-down. This is what is lacking in existing multiscale methods. The bottom-up approach is relatively straightforward, where information from microscale is properly collected and interpreted to describe macroscale phenomena. For example, a macroscale displacement field is the averaged or homogenized field from atomistic displacements, and stress and temperature fields can be calculated from atomistic forces and random velocities according to statistical mechanics. On the other hand, the top-down message passing is more challenging, and requires uncanny physical insights. In specific, we may illustrate the top-down approach through the response of a molecular system when a macroscale boundary condition such as traction is prescribed. This procedure is not trivial, because a single-scale model cannot describe both molecular system and macroscale boundary conditions. To resolve this issue, recently the present authors proposed a micromorphic multiscale molecular dynamics (MMMD) model that has intrinsic multiscale structure and multiscale dynamics (Li and Tong, 2015; Tong and Li, 2015a, 2015b; Li and Urata, 2016), which is a new type of multiscale model that attempts to rigorously resolve the relationship between molecular dynamics and continuum mechanics. The model is derived from and equivalent to classical molecular dynamics, but macroscale quantities such as traction are incorporated into microscale model versus multiscale structure design, and thus the top-down message passing becomes natural.

The present work is to further establish a multiscale coupling paradigm based on the previous multiscale molecular dynamics theory (Li and Tong, 2015; Tong and Li, 2015a). By taking advantage of the previous physical multiscale theory, an adaptive multiscale element is constructed as a messenger to translate information between regions of different scales. The message transition is smooth due to the clearly defined top-down and bottom-up characterizations. In atomistic region, molecular dynamics is the natural choice. In macroscopic region, several models can be employed depending on the

problem of interest. For example, finite element method can be used in continuum field modeling, and meshfree methods (Liu et al., 1995; Li and Liu, 2002) may be more suitable for the materials with strong nonlocal interactions. In this work, we choose peridynamics (Silling, 2000; Askari and Silling, 2005; Silling et al., 2007; Silling and Lehoucq, 2010) in macroscale modeling because that it is a nonlocal theory that has similar dynamical structure as molecular dynamics. The non-local balance law provides a seamless connection to the atomistic region. To solve the problem of spurious wave reflection in the cross-scale boundary, we introduce a filter near the interface. The procedure of filtering high-frequency wave on the interface is natural and adaptive without cumbersome ad hoc treatment. Due to the intrinsic interscale coupling property of MMMD model, mechanical quantities in different scales can be readily described and transferred among different scales without loss. The main idealogy of the proposed multiscale coupling theory is that all the multiscale coupling properties are inherently within the first-principle molecular dynamics, and we only need to explore the intrinsic properties of molecular dynamics, and do not need to develop ad hoc sophisticated coupling formulations or methods at multiscale interface as some previous multiscale methods do.

The paper is organized in four sections. Following the introduction, the framework of the multiscale computational theory is presented in Section 2. It includes the general overview of the multiscale micromorphic molecular dynamics formulation; a review of state-based peridynamics theory, and the main techniques of multiscale coupling model i.e. the transition zone or multiscale adaptive element and construction of filter, etc. Numerical algorithm is discussed subsequently. In Section 3, we present numerical examples to validate the model and find its application. The first example is an 1-D wave propagation problem, in which the process of wave transition through the interface without spurious deflection is demonstrated in this example via transition element and filtering techniques. The second example of 2-D wave propagation is then presented to further validate the multiscale coupling theory and technique. We summarize the Molecular dynamics (MD)–Peridynamics (PD) coupling theory and formulation with some discussions in the last section.

2. Multiscale coupling model

In this work, we employ the recently developed multiscale micromorphic molecular dynamics (MMMD) to model the material behaviors inside the transition zone. From historical perspective, one of the most well-known multiscale molecular dynamics is the Parrinello–Rahman molecular dynamics (PR-MD) (Parrinello and Rahman, 1981), which has been recently revisited or revised in order to connect to continuum mechanics and multiscale simulations e.g. Podio-Guidugli (2010) and Ulz (2015). The multiscale micromorphic molecular dynamics (MMMD) is a non-equilibrium generalization of the Parrinello–Rahman molecular dynamics, which is a three-scale coupled dynamics, which spans from atomistic scale to mesoscale and finally to continuum scale (Li and Tong, 2015; Tong and Li, 2015a), rigorously extending the PR-MD from an equilibrium ensemble calculation in a unit cell to a non-equilibrium molecular dynamic simulation in a finite-size domain.

The multiscale coupling model consists of three parts: atomistic region, macroscale region and a transition zone that is responsible for translating information between two regions, as shown in Fig. 1(a). The atomistic region is described by classical molecular dynamics. Interatomic potential is used to derive nonlocal forces between atoms or molecules. Materials in the macroscale region usually are required to be described by macroscale constitutive relations. Many methods can be

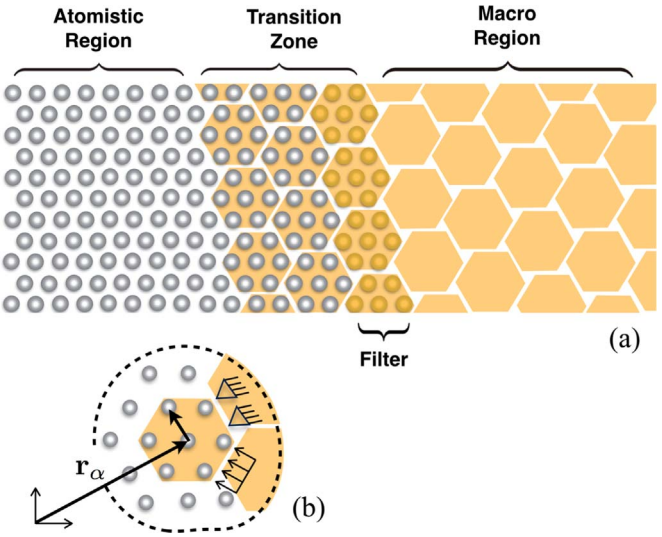

Fig. 1. (a) The multiscale model consists of three parts: atomistic region, macro region and transition zone. The essential part is the transition zone, which is served as a messenger to translate information from both regions. A filter is constructed near the interface to solve the issue of high-frequency wave reflection. (b) The adaptive multiscale element in the transition zone. This element is an assemble of atoms which has macroscale properties such as shape and average displacement while the atomistic resolution is retained. The element is capable of carrying and translating information from different scales.

chosen to establish the material model in this region depending on the problem of interest. In this work, we adopt the state-based peridynamics approach (Silling and Lehoucq, 2010), which, in principle, has similarities with molecular dynamics modeling in the fine scale region because of their similar non-local characters. To be consistent with and faithful to the atomistic modeling in the fine scale region, we adopt the Cauchy–Born rule approach to derive the macroscale constitutive relation. Hence, no empirical constitutive relation is needed. The formulation will be briefly introduced subsequently.

The essential part of the multiscale model is the transition zone. To ensure a reliable passage of information between macro and atomistic regions, several conditions need to be taken into account. First, in the bottom-up procedure, atomistic information such as force and displacement should be sensed by transition zone and interpreted to macro domain. Specifically, macroscale only receive low-frequency waves with coarse resolution, and high-frequency atomistic vibration should be filtered out otherwise it will reflect back to the atomistic region. Second, in the top-down procedure, macroscale information such as stress and deformation should also be properly interpreted to atomistic domain. The MMMD formulation (Li and Tong, 2015; Tong and Li, 2015a, 2015b) is employed here to characterize the top-down approach. The basic unit "supercell" can carry both atomistic and macroscale information, which makes it a good candidate of transition element. In this computational model, we rename it as "adaptive multiscale element". We briefly review the theory and the properties of "supercell" in the following subsection.

2.1. Microscale modeling: multiscale molecular dynamics

As shown in Fig. 1(a), between the fine scale molecular dynamics region and the coarse scale peridynamics region there is a transition zone. The transition zone has atomistic resolution same as atomistic region, however, we divide atoms in this zone into finite number of supercells. Each supercell may be viewed as a material point at macroscale, and it has a shape as an assemble of atoms. Furthermore, each atom inside the supercell is free to move as the internal degree of freedom. Having the same geometric property of the underline lattice structure, the supercell is able to describe both mesoscale and macroscale mechanical motions such as deformation and cell-level displacement. Therefore, it is possible to apply associated macroscale force field such as stress on the supercell. On the other hand, with the atomistic resolution, all information of atomistic scale is retained. As a consequence, the supercell has multiscale structure and property. A detailed extensive discussion of MMMD and how to construct the supercell size can be found in Li and Tong (2015) and Tong and Li (2015a). In the following, we briefly summarize the basic theory and formulations of MMMD, and a detailed exposition of MMMD theory is presented in Appendix.

In MMMD, the atomistic position $\mathbf{r}_i(t)$ in the current configuration is composed of the following parts:

$$\mathbf{r}_i(t) = \mathbf{r}_\alpha(t) + \boldsymbol{\phi}_\alpha(t)\cdot\mathbf{S}_i(t), \tag{1}$$

where $\mathbf{r}_\alpha$ is the center of mass of α-th supercell calculated as,

$$\mathbf{r}_\alpha = \frac{\sum_{i\in S_\alpha} m_i\mathbf{r}_i}{\sum_{i\in S_\alpha} m_i}, \tag{2}$$

with m_i being the mass of i-th atom inside the α-th cell, and S_α is the index set of all atoms inside the α-th cell. From the perspective of a single cell, the motion of the center of mass may represent the rigid body translation of the supercell. However, the aggregated motion of all centers of mass of every supercells describes the coarse scale deformation at the continuum level. In Eq. (1), $\boldsymbol{\phi}_\alpha$ is the total deformation gradient of α-th cell, and it is uniform throughout the cell. $\mathbf{S}_i$ is the internal degree of freedom which represents the atomistic distribution inside the cell. $\boldsymbol{\phi}_\alpha\cdot\mathbf{S}_i$ is the relative position comparing to the center of mass. This operation is different from the uniform deformation described by the Cauchy–Born rule, and it is a multiscale micromorphic deformation (Li and Tong, 2015). In fact, $\boldsymbol{\phi}_\alpha$ can be further decomposed to

$$\boldsymbol{\phi}_\alpha(t) = \mathbf{F}_\alpha(t)\cdot\boldsymbol{\chi}_\alpha(t), \tag{3}$$

where $\mathbf{F}_\alpha$ is related to macroscale continuum deformation depending on the distribution or the aggregated motion of centers of mass of supercells (Tong and Li, 2015a); whereas $\boldsymbol{\chi}_\alpha$ is an independent mesoscale deformation tensor for each supercell (or for the representative α-th supercell), which includes local stretch and local rotation. By introducing the center of mass and deformation gradient for supercells, each supercell obtains the properties of a material point in macroscale continuum mechanics. The internal degrees of freedom is then enable the interaction between particles from atomistic domain.

In passing, we note that Eq. (3) is a form of *multiplicative decomposition* of the deformation gradient into multiscale components, and it is coined as the *multiplicative multiscale decomposition* (Li and Urata, 2016), which is in contrast to the multiscale addictive decomposition proposed by Wagner and Liu (2003). It is also a reminiscence of the multiscale decomposition in elasto-plasticity theory by Lee (1969).

We denote

$$\mathbf{R}_\alpha := \mathbf{r}_\alpha(0) \quad \text{and} \quad \mathbf{R}_i = \mathbf{R}_\alpha + \boldsymbol{\phi}(0)\mathbf{S}_i(t).$$

Note that the time variable in that variable $\mathbf{S}_i(t)$ has different time scale with the time variable in both $\mathbf{r}_\alpha(t)$ and $\boldsymbol{\chi}(t)$, so that we do not need to initialize it for the computational purpose. One may further define an intermediate position or configuration,

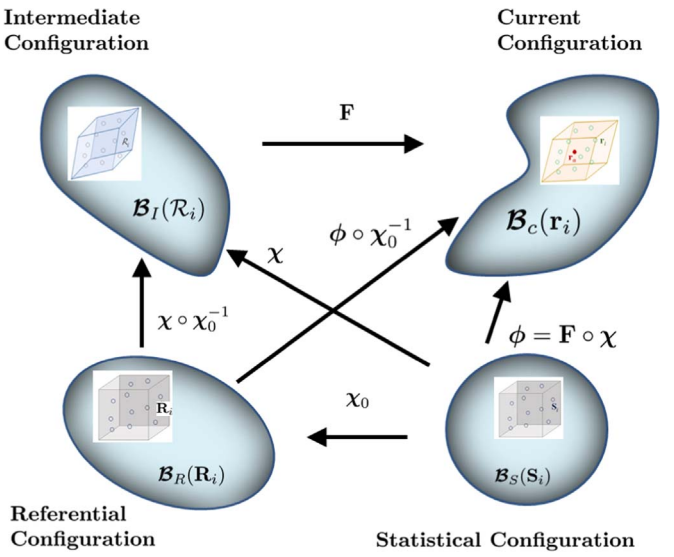

Fig. 2. Different configuration spaces in multiscale micromorphic molecular dynamics.

$$\mathcal{R}_i := \mathbf{R}_\alpha + \chi(t)\cdot\mathbf{S}_i(t), \quad \text{with } \boldsymbol{\phi}_\alpha(\mathcal{R}) = \mathbf{F}_\alpha(0)\chi_\alpha(t) = \chi(t), \quad \mathbf{F}_\alpha(0) = \mathbf{I}.$$

This intermediate configuration distinguishes the time scales in mesoscale and macroscale variables. A complete kinematic relations and mappings are illustrated in Fig. 2, and readers may find more detailed discussions on different configurational spaces in Li and Tong (2015).

To construct a discrete nonlocal deformation gradient, we first associate a compact support with each center of mass of a supercell, say the α-th cell. Then we can construct a shape tensor for each horizon that is based on the distribution of all centers of mass inside the compact support of the center of mass of α-th cell, i.e.

$$\mathbf{K}_\alpha := \int_{\mathcal{H}_{\mathbf{R}_\alpha}} \omega(|\mathbf{R}_\alpha|)\mathbf{R}_{\alpha\beta} \otimes \mathbf{R}_{\alpha\beta} dV_\beta \approx \sum_{\beta \in S_N} \omega(|\mathbf{R}_\alpha|)\mathbf{R}_{\alpha\beta} \otimes \mathbf{R}_{\alpha\beta}\Delta V_\beta \tag{4}$$

where $\mathbf{R}_{\alpha\beta} = \mathbf{R}_\beta - \mathbf{R}_\alpha$, and S_N is the index set for all the centers of supercells that are inside $\mathcal{H}_{\mathbf{R}_\alpha}$. The shape tensor is basically a moment tensor or loosely speaking a moment of inertia tensor. Note that there is no difference between $\mathbf{R}_\alpha$ and $\mathcal{R}_\alpha$.

One can then define a two point nonlocal second order tensor $\mathbf{N}_\alpha$ as

$$\mathbf{N}_\alpha = \int_{\mathcal{H}_{\mathbf{R}_\alpha}} \omega(|\mathbf{R}_\alpha|)\mathbf{r}_{\alpha\beta} \otimes \mathbf{R}_{\alpha\beta} dV_\beta \approx \sum_{\beta=1}^{N} \omega(|\mathbf{R}_\alpha|)\mathbf{r}_{\alpha\beta} \otimes \mathbf{R}_{\alpha\beta}\Delta V_\beta, \tag{5}$$

where $\mathbf{r}_{\alpha\beta} = \mathbf{r}_\beta - \mathbf{r}_\alpha$. At the coarse scale, we assume that the following Cauchy–Born rule is hold in each compact support of the center of mass of the supercell (see Fig. 12),

$$\mathbf{r}_{\alpha\beta} = \mathbf{F}_\alpha \mathbf{R}_{\alpha\beta}. \tag{6}$$

By substituting Eq. (6) into (5), we obtain the expression for the discrete non-local deformation gradient,

$$\mathbf{F}_\alpha = \mathbf{N}_\alpha \mathbf{K}_\alpha^{-1} = \int_{\mathcal{H}_{\mathbf{R}_\alpha}} \left(\omega(|\mathbf{R}_\alpha|)\mathbf{r}_{\alpha\beta} \otimes \mathbf{R}_{\alpha\beta} dV_\beta \right) \mathbf{K}_\alpha^{-1} \approx \left(\sum_{\beta=1}^{N} \omega(|\mathbf{R}_\alpha|)\mathbf{r}_{\alpha\beta} \otimes \mathbf{R}_{\alpha\beta}\Delta V_\beta \right) \mathbf{K}_\alpha^{-1}. \tag{7}$$

The mechanical boundary of an MMMD supercell is shown in Fig. 1(b), and it is also shown in Fig. 13 in a more general setting. The force fields from different scales drive the motions of each supercell. The first field is from the atomistic interaction among different atoms that are within each supercell or from different supercells. The second interaction is the external stress or traction acting on the interface exerted from the macroscale region. We characterize these two external forces by the following potential energies:

$$V_\alpha^{atom} = \sum_{i \in \alpha, j \notin \alpha} \varphi(r_{ij}) \tag{8}$$

$$V_\alpha^{surf} = -S_\alpha^0 \bar{\mathbf{t}}_\alpha^0 \cdot \mathbf{r}_\alpha \tag{9}$$

where $i \in \alpha$ and $j \in \beta$ are indices of the atoms from different cells ($\alpha \neq \beta$; ϕ is the pair potential, and r_{ij} is the distance

between i-th and j-th atoms, and S_α^0 is the surface exerted by the traction $\bar{\mathbf{t}}_\alpha^0$, which is in the referential configuration.

Thus the total potential energy from outside the α-cell is

$$V_\alpha^{ext} = V_\alpha^{atom} + V_\alpha^{surf}. \tag{10}$$

On the other hand, the potential energy inside the α-th cell, V_α^{atom}, is

$$V_\alpha^{int} = \frac{1}{2}\sum_{i,j\in S_\alpha} \varphi(r_{ij}), \tag{11}$$

where the indices i and j represent different atoms within the same cell, and hence there is an $\frac{1}{2}$ factor. S_α is the index set for all the atoms inside the supercell α.

The kinetic energy can be calculated based on the multiscale kinematic decomposition (Eq. (1)) as discussed in Li and Tong (2015) and Tong and Li (2015a),

$$K_\alpha = \frac{1}{2}\sum_{i\in S_\alpha} m_i\dot{\mathbf{r}}_i\cdot\dot{\mathbf{r}}_i = K_\alpha^{rigid} + K_\alpha^{cell} + K_\alpha^{atom} = \frac{1}{2}M_\alpha\dot{\mathbf{r}}_\alpha\cdot\dot{\mathbf{r}}_\alpha + \frac{1}{2}\dot{\boldsymbol{\phi}}_\alpha^T\dot{\boldsymbol{\phi}}_\alpha : \mathbf{J}_\alpha + \frac{1}{2}\mathbf{C}_\alpha : \sum_{i\in S_\alpha} m_i\dot{\mathbf{S}}_i\otimes\dot{\mathbf{S}}_i, \tag{12}$$

where M_α is the mass of the whole cell; $\mathbf{C}_\alpha = \boldsymbol{\phi}_\alpha^T\boldsymbol{\phi}_\alpha$ is the right Cauchy–Green tensor, and $\mathbf{J}_\alpha = \sum_{i\in S_\alpha} m_i\mathbf{S}_i\otimes\mathbf{S}_i$ is the moment inertia tensor, which is approximated as a constant spherical tensor that is independent from time. The above kinetic energy is slightly different from the original molecular dynamics kinetic energy from first principle. However, the additional terms are dropped out because of imposed statistical constraints. Readers may find the detailed discussion in Li and Tong (2015) and Tong and Li (2015a).

The Lagrangian for α-th supercell can then be written as,

$$\begin{aligned}\mathcal{L}_\alpha &= K_\alpha - V_\alpha\\ &= K_\alpha^{rigid} + K_\alpha^{cell} + K_\alpha^{atom} - V_\alpha^{int} - V_\alpha^{ext}\\ &= \frac{1}{2}M_\alpha\dot{\mathbf{r}}_\alpha\cdot\dot{\mathbf{r}}_\alpha + \frac{1}{2}\dot{\boldsymbol{\phi}}_\alpha^T\dot{\boldsymbol{\phi}}_\alpha\\ &\quad : \mathbf{J}_\alpha + \frac{1}{2}\mathbf{C}_\alpha : \sum_{i\in S_\alpha} m_i\dot{\mathbf{S}}_i\otimes\dot{\mathbf{S}}_i - \frac{1}{2}\sum_{i,j\in S_\alpha}\varphi\left(r_{ij}\right) - \sum_{i\in S_\alpha, j\notin S_\alpha}\varphi\left(r_{ij}\right) + S_\alpha^0\bar{\mathbf{t}}_\alpha^0\cdot\mathbf{r}_\alpha.\end{aligned} \tag{13}$$

The above Lagrangian has independent variables $\mathbf{r}_\alpha$, $\boldsymbol{\phi}_\alpha$ (or χ_α) and $\mathbf{S}_i$. Through the standard derivation procedure (see Appendix), the equations of motion for these variables are obtained as,

$$M_\alpha\ddot{\mathbf{r}}_\alpha = \sum_{i\in S_\alpha, j\notin S_\alpha}\mathbf{f}_{ij} + S_\alpha^0\bar{\mathbf{t}}_\alpha^0; \tag{14}$$

$$\ddot{\boldsymbol{\phi}}_\alpha\cdot\mathbf{J}_\alpha = \left(\mathcal{P}_\alpha^{ext} - \mathcal{P}_\alpha^{int}\right)\Omega_\alpha^0; \tag{15}$$

$$m_i\mathbf{C}_\alpha\cdot\ddot{\mathbf{S}}_i = \sum_j \mathbf{f}_{ij}\cdot\boldsymbol{\phi}_\alpha - m_i\dot{\mathbf{C}}_\alpha\cdot\dot{\mathbf{S}}_i, \tag{16}$$

where $\mathbf{f}_{ij}$ is the interaction force on i-th atom from j-th atom; Ω_α^0 is the volume of the supercell in the referential configuration, and

$$\mathcal{P}_\alpha^{int} = \frac{1}{\Omega_\alpha^0}\left(\frac{1}{2}\sum_{i,j\in S_\alpha}\mathbf{f}_{ij}\otimes\mathbf{S}_{ij} - \boldsymbol{\phi}_\alpha\cdot\sum_{i\in S_\alpha} m_i\dot{\mathbf{S}}_i\otimes\dot{\mathbf{S}}_i\right) \tag{17}$$

$$\mathcal{P}_\alpha^{ext} = \frac{1}{\Omega_\alpha^0}\sum_{i\in\alpha, j\notin S_\alpha}\mathbf{f}_{ij}\otimes\mathbf{S}_i. \tag{18}$$

They are defined as the internal and external first Piola–Kirchhoff (PK-I) stresses. Note that both internal and external Piola–Kirchhoff stresses defined in Eqs. (17) and (18) are two point tensors. However, they are defined in the configuration space $\mathcal{B}_c(\mathbf{r}_i)\times\mathcal{B}_S(\mathbf{S}_i)$ rather than in the configuration space $\mathcal{B}_c(\mathbf{r}_i)\times\mathcal{B}_R(\mathbf{R}_i)$ nor in the configuration space $\mathcal{B}_c(\mathbf{r}_i)\times\mathcal{B}_I(\mathcal{R}_i)$ (see Fig. 2). Hence

$$\mathcal{P}_\alpha^{int} \neq \left.\frac{\partial W}{\partial\mathbf{F}}\right|_{\mathbf{F}=\mathbf{F}_\alpha}.$$

The multiscale equations of motion have the general form of $\tilde{M}\ddot{\mathbf{q}} = \tilde{\mathbf{F}}$. The general masses are M_α, $\mathbf{J}_\alpha$ and $m_i\mathbf{C}_\alpha$ for three equations of motion, respectively. The general kinematic displacements are $\mathbf{r}_\alpha$, χ_α or $\boldsymbol{\phi}_\alpha$, and $\mathbf{S}_i$.

The driving force for the motion of the centers of mass of supercells, $\mathbf{r}_\alpha$, consists of two parts: (1) from atomistic

interaction among different supercells, and (2) from macroscale surface traction or body force. The deformation of the cell is driven by external PK-I stress while resisted by internal PK-I stress. Internal motion is induced by atomistic interactions and damped, if macroscale velocity $\dot{\mathbf{C}}_\alpha$ exists. It may be noted that the MMMD formulation outlined here is not an ad hoc multiscale numerical construction. Instead, it has rigorous molecular physics and statistical mechanics foundation. To help readers to understand MMMD formulation, a detailed derivation of MMMD formulation is provided in Appendix.

The adaptive nature of the supercell is due to its capability of carrying information or transporting boundary flux at different scales. The atomistic interaction influences motions of all scales including rigid body motions, deformation and internal degree of freedom fluctuation as seen in Eqs. (14)–(16), while macroscale information such as traction and average displacement can be readily applied to Eq. (14). Moreover, we can apply an equilibrium stress state on a supercell by replacing $\mathcal{P}_\alpha^{ext}$ in Eq. (15) with a prescribed value $\bar{\mathcal{P}}_\alpha^{ext}$. Therefore, the adaptive multiscale element is a good candidate as a messenger in transition zone for the multiscale model.

2.2. Macroscale modeling: peridynamics

Peridynamics (Silling, 2000; Askari and Silling, 2005; Silling et al., 2007; Silling and Lehoucq, 2010) is a nonlocal computational formulation of continuum mechanics. From multiscale perspective, it may be viewed as a coarse grain model. Different from classical continuum mechanics, in peridynamics, the interaction between material points is nonlocal, i.e. for a fixed material point $\mathbf{r}_\alpha$ in the current configuration, it can interact with neighboring particles $\mathbf{r}_\beta$ within a compact support called as *horizon*, which is similar to the concept of cutoff range in molecular dynamics. Here we denote the material point of interest as α to be consistent with the center of mass in an adaptive multiscale element, and all other particles in the horizon as $\beta = 1, 2, \ldots, N$. The uppercase is used to denote the quantities in the referential configuration. $\mathcal{H}_{\mathbf{R}_\alpha}$ is used to denote the horizon. Interactions from material points outside the horizon are set to zero. The deformation state of a material point is characterized by discrete nonlocal deformation gradient tensor $\mathbf{F}_\alpha(\mathbf{R}_\alpha, t)$, which is adopted the coarse scale deformation gradient for the centers of mass of the supercells defined in Eqs. (4)–(7).

Considering the state-based peridynamics, we denote the force state at material point α as $\mathbf{T}_\alpha\langle\mathbf{R}_\beta - \mathbf{R}_\alpha\rangle$. Assume that there exists a macroscale free-energy density at the material point α, i.e. $\Psi(\mathbf{X}^\alpha)$. Then the virtual work or the variation of the free energy density may be written as,

$$\delta\Psi(\mathbf{R}^\alpha) = \mathbf{P}_\alpha : \delta\mathbf{F}_\alpha = \mathbf{P}_\alpha : \int_{\mathcal{H}_{\mathbf{R}^\alpha}} \omega(|\mathbf{R}_{\alpha\beta}|)\delta\mathbf{r}_{\alpha\beta} \otimes \mathbf{R}_{\alpha\beta} dV_\beta \mathbf{K}_\alpha^{-1} = \int_{\mathcal{H}_{\mathbf{R}^\alpha}} \mathbf{T}_\alpha\langle\mathbf{R}_\beta - \mathbf{R}_\alpha\rangle \cdot \delta\mathbf{r}_{\alpha\beta} dV_\beta, \tag{19}$$

which leads to the force state expression (see Silling and Lehoucq, 2010) that is determined by the local stress state at the given material point α, i.e.,

$$\mathbf{T}_\alpha\langle\mathbf{R}_\beta - \mathbf{R}_\alpha\rangle = \omega(|\mathbf{R}_\alpha|)\mathbf{P}_\alpha \cdot \mathbf{R}_{\alpha\beta}\mathbf{K}_\alpha^{-1}, \tag{20}$$

where $\mathbf{P}_\alpha$ is the coarse scale first Piola–Kirchhoff stress at the material point α.

To find the local stress, we employ the atomistic potential of the underline solid and the Cauchy–Born rule. Since this is the coarse scale calculation, we assume that each peridynamics point is associated with an atomistic unit cell (see Fig. 3). For illustration purpose, we assume that the elastic energy density at each peridynamics point may be expressed as a pair potential in a Bravais lattice,

$$W = \frac{1}{2\Omega_0}\sum_{k=1}^{N_b} \varphi(r_k), \tag{21}$$

where Ω_0 is the volume of the unit cell, and inside Ω_0 there are total N_b number of bonds connecting to the center atom. $\varphi(r_k)$ is the atomistic potential of k-th bond, and r_k is the atomistic bond length in the deformed configuration. $k = 1,\ldots,N_b$,

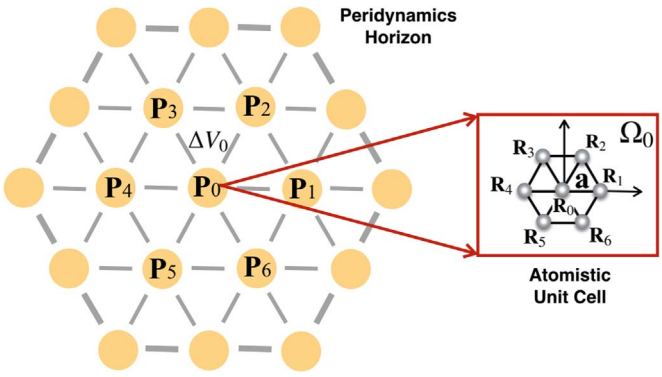

Fig. 3. The Cauchy–Born rule based multiscale peridynamics.

with N_b being the number of bonds in a unit cell. Based on the Cauchy–Born rule, we can calculate the first Piola–Kirchhoff stress by taking derivative of elastic energy density with respect to deformation gradient,

$$\mathbf{P}_\alpha = \left.\frac{\partial W}{\partial \mathbf{F}}\right|_{\mathbf{F}=\mathbf{F}_\alpha} = \frac{1}{2\Omega_0}\sum_{k=1}^{N_b}\varphi'(r_k)\frac{\mathbf{r}_k\otimes\mathbf{R}_k}{r_k}, \tag{22}$$

where $\mathbf{r}_k$ and $\mathbf{R}_k$ are bond vectors in the current and the referential configurations, respectively. The Cauchy–Born rule implies that $\mathbf{r}_k = \mathbf{F}_\alpha\cdot\mathbf{R}_k$. Therefore, if the deformation gradient is given, we can calculate the first Piola–Kirchhoff stress at the macroscale material point α. Different from Eqs. (17) and (18), the Piola–Kirchhoff stress expressed in Eq. (22) is defined in the macroscale counterpart of the configurational space $\mathcal{B}_c(\mathbf{r}_i)\times\mathcal{B}_R(\mathbf{R}_i)$.

The Cauchy–Born rule based stress evaluation avoids the empirical constitutive relations introduced in macroscale continuum mechanics. Therefore, less artifacts are expected in the proposed multiscale model.

After determining the stress state at every peridynamics particles, we can establish a unified equation of motions for peridynamics based on the so-called state-based peridynamics formulation. Considering the balance of linear momentum at the material point $\mathbf{r}_\alpha$, we have the following nonlocal balance equation:

$$\rho_\alpha\ddot{\mathbf{r}}_\alpha = \mathbf{L}(\mathbf{R}_\alpha, t) + \rho_\alpha\mathbf{b}(\mathbf{R}_\alpha) \tag{23}$$

where

$$\mathbf{L}(\mathbf{R}_\alpha, t) = \int_{\mathcal{H}_\alpha}(\mathbf{T}_\alpha\langle\mathbf{R}_\beta-\mathbf{R}_\alpha\rangle - \mathbf{T}_\beta\langle\mathbf{R}_\alpha-\mathbf{R}_\beta\rangle)dV_\beta \tag{24}$$

is the nonlocal stress divergence vector acting on the α-th material point by neighboring macroscale points β. Its counterpart in classical continuum mechanics is $\nabla_{\mathbf{R}}\cdot\mathbf{P}_\alpha$, which is a local divergence term. Again, here $\mathbf{P}_\alpha$ is the first Piola–Kirchhoff stress tensor in continuum mechanics. Mathematically, the requirements on the solution of an integral equation are much less than that of a differential equation. To solve Eq. (24), one mainly need to evaluate the nonlocal force density vector or the nonlocal divergence vector $\mathbf{L}(\mathbf{R}_\alpha, t)$. In computation implementation, since the domain is discretized into many material points, the integral can be replaced or approximated by the following summation,

$$\mathbf{L}(\mathbf{R}_\alpha, t) = \sum_{\beta=1}^{N}(\mathbf{T}_\alpha\langle\mathbf{R}_\beta-\mathbf{R}_\alpha\rangle - \mathbf{T}_\beta\langle\mathbf{R}_\alpha-\mathbf{R}_\beta\rangle)\Delta V_\beta. \tag{25}$$

2.3. Construction of the filter

A common issue of multiscale methods is the reflection of high-frequency waves at the multiscale interface. Due to the larger discretization spacing in the macroscale region, high-frequency wave components cannot be captured, and, as a result of energy conservation, high-frequency signals will be reflected back to the atomistic region. The issue of reflection is demonstrated in Fig. 4. When the wave passes the multiscale interface, the low-frequency wave transits through smoothly, whereas the high-frequency wave cannot, and its reflection back to the fine scale region can be clearly observed. Note that high and low frequencies are relative concepts compared with lattice spacings of both atomistic and macro domain. The

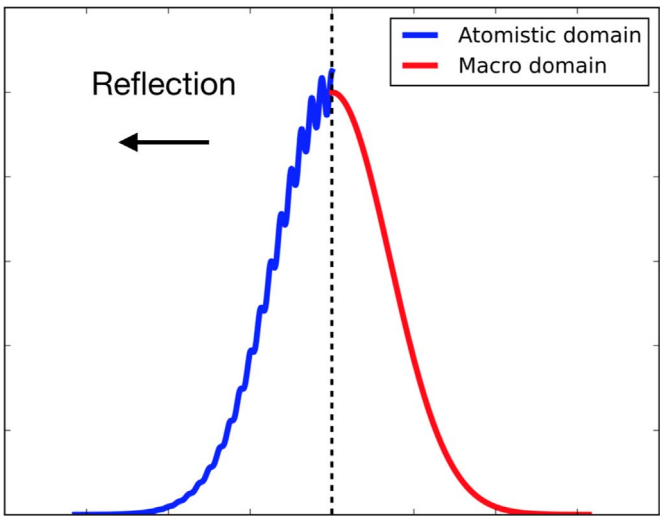

Fig. 4. Illustration of wave reflection at multiscale interface. Due to the large discretization spacing, the macro region cannot capture the high-frequency incident wave. If the total energy is conserved without releasing, these high-frequency wave components will reflect back to the atomistic region.

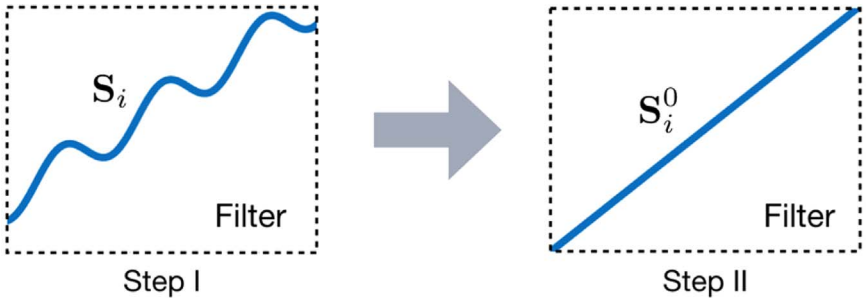

Fig. 5. Construction of the filter. Step I: The filter has the same function as transition element, where all wave components propagate into the element. Step II: Homogenization. Displacements are averaged inside the filter. In practice, we set the internal variable $\mathbf{S}_i$ to its initial value $\mathbf{S}_i^0$, which produces a uniform total deformation.

term low frequency used here means that the associated wavelength is larger than the discretization spacing of the coarse scale region, while the high frequency means that the associated wavelength is in between the intrinsic lattice spacing in fine scale region and the discretization spacing of the macroscale domain.

To resolve the issue of the discretization-induced spurious reflection, we introduce a filter in the transition zone near the surface of macro domain as demonstrated in Fig. 1(a). The filter is similar as transition element in shape, and it is also an assemble of atoms. The construction of the filter includes two steps as shown in Fig. 5. First, we allow all wave components enter the filter. In this step, the filter is basically the same as transition element, where atoms in the filter are free to move as any transition element. The motion is controlled by original dynamical equations (14)–(16). The second step is a process of homogenization. The atomistic positions are set to an average value. The microscale fluctuation $\mathbf{S}_i$ is to be replaced by its chosen initial value $\mathbf{S}_i^0$. Thus the homogenized atomistic position becomes,

$$\mathbf{r}_i = \mathbf{r}_\alpha + \boldsymbol{\phi}_\alpha \cdot \mathbf{S}_i^0. \tag{26}$$

The replacement is effective in Eqs. (14)–(15), and Eq. (16) is eliminated. It is equivalent to freeze the internal degrees of freedoms, and only macroscale motions are allowed, i.e. motions of particles are adhered on the macroscale deformation of the supercell. This process may be understood as an energy release process. The interesting fact of the adaptive multiscale element is that we can lock any of the three scale variables to meet the need of different resolutions. The treatment of directly sweeping the high frequency components is brute but effective. When the waves pass the filter, a “smooth” wave with narrow bandwidth replaces the broadband incident waves. Theoretically, all high-frequency waves are expected to be filtered out while the low-frequency components are transmitted to the macro domain. We will demonstrate the process in the numerical examples.

2.4. Numerical implementation

We now introduce the transition zone that is designed to transfer information between two different scales or regions. In a mechanical system, force-stress and displacement-strain are two basic sets of quantities. As discussed in the last section, the adaptive multiscale element is capable of carrying all these information from both scales or both regions. Thus the message translation can be made seamless passing through adaptive multiscale element with little numerical distortion. In the following, we briefly discuss the two options of message passing on the multiscale interphase as follows:

(1) *Traction-force match*: In this case, the transition zone is a separated interphase that joins atomistic region and macroscale region together. The traction from macroscale domain acts on the center of mass of the transition elements, while at the same time the stress developed in the transition elements will exert the force on the material particles at boundary of the macroscale domain as a form of applied traction or reaction.

Both action and reaction have the form of macroscale traction, which are incorporated in Eq. (14). On the other side, atomistic domain interacts with transition zone by exerting atomistic forces. The procedure is concurrent in time, i.e. particle motions in three different domains evolve at the same time.

(2) *Displacement match*: In this case, the transition zone can be treated as an overlap of both macro and atomistic domains. In MD updates, the transition elements are parts of atomistic domain, and the centers of mass of the supercells are automatically updated due to the global motion of the assemble (element). The updated centers of mass are then passed to the macro domain as displacement boundary condition. Similarly, the updated macroscale displacements are used by transition elements as centers of mass, while the shape and internal variables are still free to move, as governed by Eqs. (15)–(16). Meanwhile, the atomistic region updates based on the new atomic positions in transition zone.

An appropriate integration scheme is needed for updating the quantities and facilitating exchange of information. The advantage of the multiscale structure is not only in space but also in time. An efficient strategy is choosing larger time steps for macroscale and smaller steps for atomistic scale. There are two levels of computational cycles. The microscale and macroscale regions are on the first level. Based on different approaches of force-traction or displacement interchange, parallel and serial algorithms can be used separately (see Tong and Li, 2015a). On the second level, three kinematic

quantities are in the adaptive multiscale element in transition zone: $\mathbf{r}_\alpha$, $\boldsymbol{\phi}_\alpha$ and $\mathbf{s}_i$. Therefore, we have five variables at different scales, whose combinations may provide some flexibility for choosing step sizes during time integration. Both parallel and serial algorithms are applicable on the second level based on different conditions and requirements. The velocity Verlet method (Verlet, 1967) and the predictor–corrector method (Gear, 1971) are among the most popular integrators in time integration. In this work, we employ both of them in the multiscale time integration. The velocity Verlet method is used in calculating displacement fields in atomistic region, macroscale region, and for the centers of mass $\mathbf{r}_\alpha$ in transition elements. The predictor–corrector method is used to update $\boldsymbol{\phi}_\alpha$ and $\mathbf{s}_i$ in transition elements. As an example, the MD update is formulated as follows:

$$\mathbf{r}_i^{n+1} = \mathbf{r}_i^n + \dot{\mathbf{r}}_i^n \Delta t_{\mathbf{r}_i} + \frac{1}{2}\ddot{\mathbf{r}}_i^n \Delta t_{\mathbf{r}_i}^2, \tag{27}$$

$$\ddot{\mathbf{r}}_i^{n+1} = \mathbf{f}_i^{n+1}(\mathbf{r}_i^{n+1})/m_i, \tag{28}$$

$$\dot{\mathbf{r}}_i^{n+1} = \dot{\mathbf{r}}_i^n + \frac{1}{2}\left(\ddot{\mathbf{r}}_i^n \Delta t_{\mathbf{r}_i} + \ddot{\mathbf{r}}_i^{n+1} \Delta t_{\mathbf{r}_i}\right). \tag{29}$$

In the second step, we need to evaluate force field based on the new position $\mathbf{r}_i^{n+1}$. For the centers of mass of the transition element and the macroscale material points, we may simply replace $\mathbf{r}_i$ by $\mathbf{r}_\alpha$ in the above equations. However, the size of the time step and magnitude of the mass should be changed accordingly.

We summarize the general procedure of implementation in the following table:

Table 1. Multiscale computation algorithm (flow chart).

- Determine the specific problem of interest, e.g. wave or crack propagation, etc.
- Set up parameters of the system, e.g. material, model dimension, time steps, etc.
- Initialize the whole system: initial displacement, velocity, boundary condition, etc.
- Select the type of communication: force-traction/displacement.
- Update atom motions in atomistic region: the velocity-Verlet by Eqs. (27)–(29).
- Update atom motions in transition zone:
  - Velocity-Verlet for $\mathbf{r}_\alpha$ in Eq. (14);
  - Predictor–corrector for $\boldsymbol{\phi}_\alpha$ and $\mathbf{s}_i$ in Eqs. (15)–(16);
- Update particle motions in macroscale region: Velocity-Verlet by Eqs. (27)–(29).
- Exchange of information:
  - Force-traction: **atomic forces ⇌ transition elements ⇌ macroscale traction**
  - Displacement: **atomistic displacements → transition zone → macro displacements →transition zone → atomistic displacements**

3. Numerical examples

In this section, we present the results of two numerical tests to validate the proposed multiscale coupling method, which are 1-D and 2-D wave propagation problems. The pairwise Morse potential is used to model the interaction force between atoms, which is given as,

$$\varphi(r) = D(e^{-2\alpha(r-r_0)} - 2e^{-\alpha(r-r_0)}) \tag{30}$$

The pair force is derived as

$$f(r) = -\frac{\partial \phi(r)}{\partial r} = 2D\alpha(e^{-2\alpha(r-r_0)} - e^{-\alpha(r-r_0)}) \tag{31}$$

where the constants D=0.0965 eV, α=2.71/Å and r_0=2.878 Å.

3.1. 1-D wave propagation

In the 1-D example problem, aluminum with an atomic weight of 26.98 u is selected as the material under studying. The lattice space is a_0=2.878 Å. Each adaptive multiscale element has 5 atoms, and each peridynamic material point is chosen the same size of the multiscale element. The atomistic region consists of 475 atoms. Five multiscale elements are located in the transition zone. A total 150 material points are assigned to the macro region. The model is shown in Fig. 6. An initial Gaussian displacement is applied as

$$u(x, t=0) = \begin{cases} Ae^{-\frac{x^2}{2\sigma^2}}\left(1 + b\cos\left(\frac{2\pi x}{H}\right)\right) & x \le L_c \\ 0 & x > L_c \end{cases} \tag{32}$$

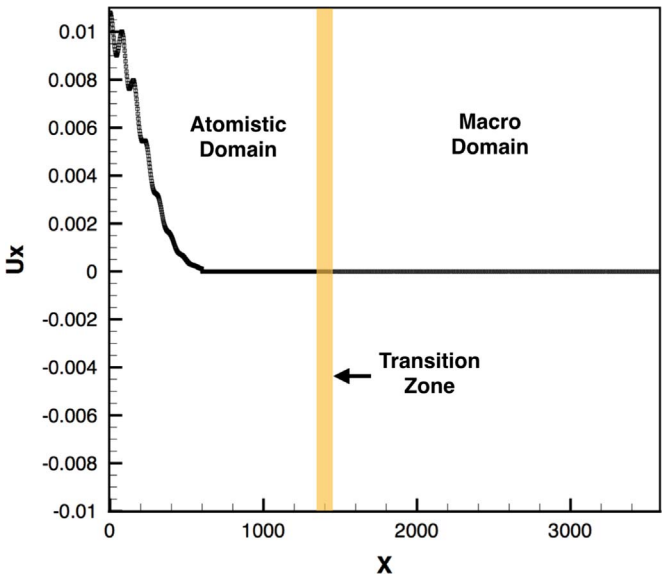

Fig. 6. 1-D model setup with a Gaussian initial displacement of magnitude 0.01. From left to right: atomistic domain ($0 \le x < 1367$), transition zone ($1367 \le x < 1439$) and macro domain ($1439 \le x < 3598$). All units are in angstrom.

with $A=0.01$, $\sigma=200$, $b=0.08$, and $H=\sigma/2$, in angstrom. The initial displacement is truncated at $L_c = 4\sigma$. The exponential term in Eq. (32) is the low-frequency wave which is expected to pass through the transition zone to the macro region. The cosine term is the high-frequency component, which should be appropriately filtered, and the associated energy should be released. Time steps for atomistic and macro regions are $\Delta t_a = 0.001$ and $\Delta t_m = 0.006$, respectively. For the transition elements, time steps are chosen as $\Delta t_s = 0.001$, $\Delta t_\phi = 0.002$ and $\Delta t_r = 0.002$. All units are in picosecond. The above selection of time step sizes is just an example. Practically, different combinations can be considered as long as they are fully tested to avoid rush or lag in time between different regions. During the updates, each scale or region includes several sub-steps. The numbers of other sub-step values have been tested to ensure smooth transition.

Fig. 7(a) and (b) show the history of wave propagation without filter in transition zone. Within 2250 macroscale time steps, the entire wave motion is in the atomistic domain, and we can clearly distinguish the low- and high- frequency components of the wave. When the wave propagates to the macro domain, the low-frequency wave has almost entirely been transmitted. However, without filter, the high-frequency component is reflected back to the atomistic domain since the mismatch of impedances at the multiscale boundary.

As mentioned in the previous section, constructing a filter is straightforward, because it is simply an element with frozen fine scale motions. In this example, we choose a set of three multiscale elements in the transition zone as filters. Fig. 8 shows the location of the wave at $t = 5000\Delta t_m$, when filter is turned on. Comparing with Fig. 7(b), one may find that the reflection

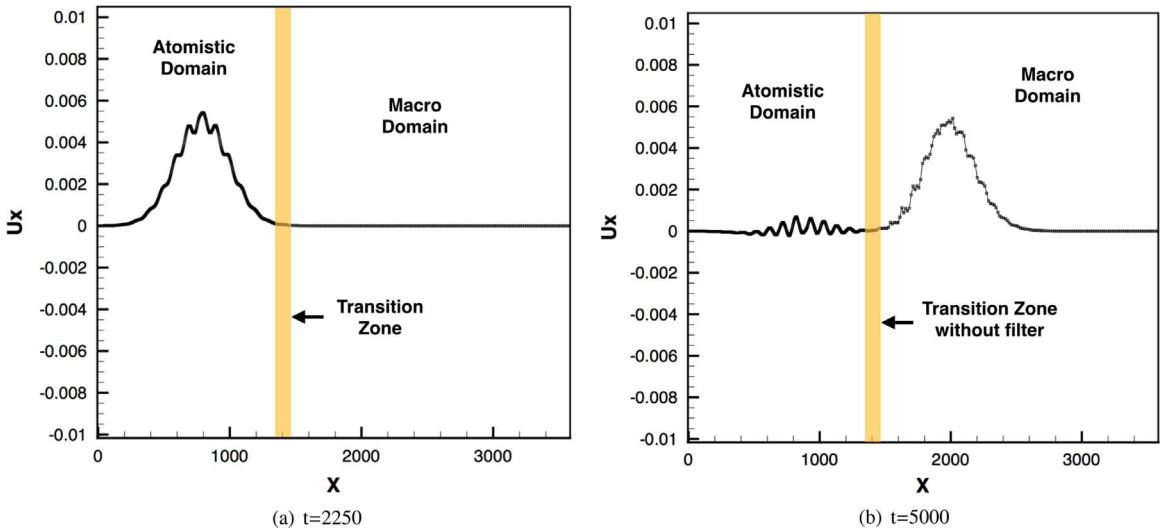

(a) t=2250 (b) t=5000

Fig. 7. Displacement at (a) $t=2250$ and (b) $t=5000$ with units of macroscale step size Δt_m. No filter is placed in the transition zone.

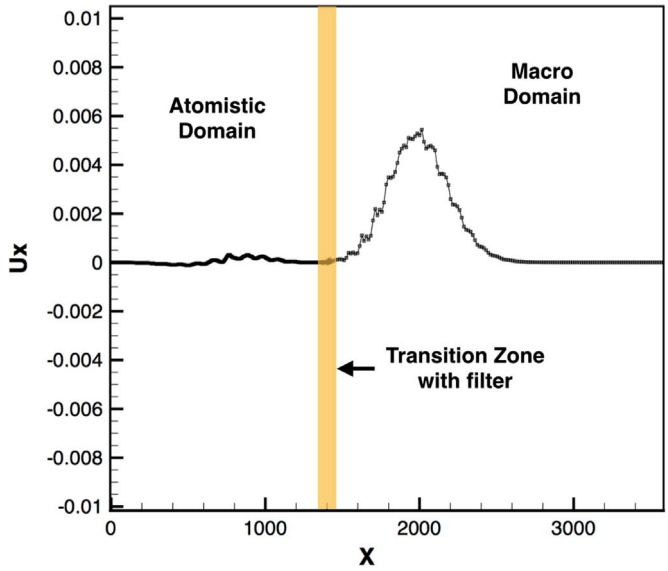

Fig. 8. Displacement at $t = 5000\Delta t_m$ with filter in the transition zone.

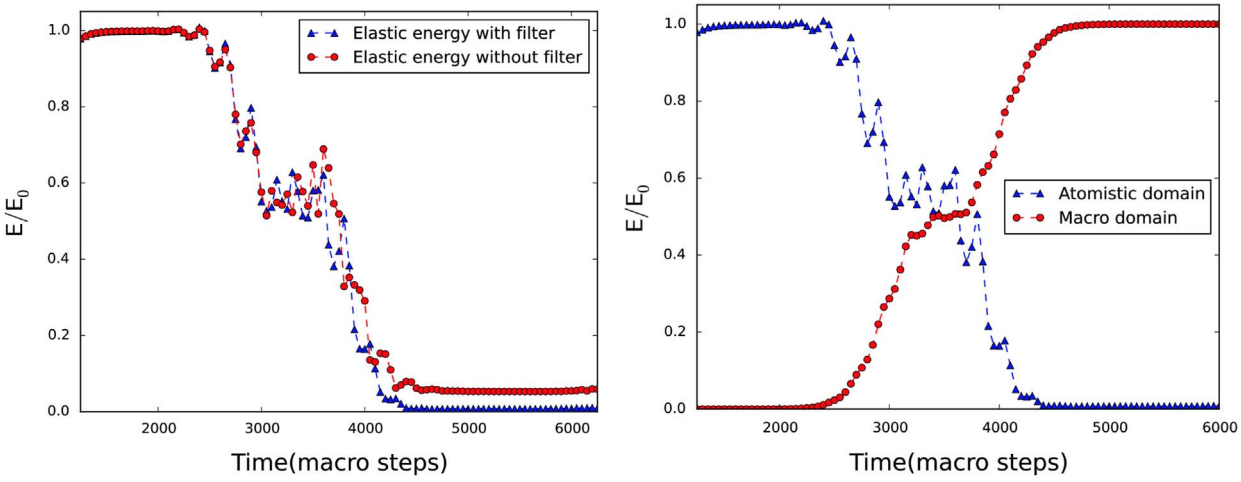

(a) Energies of atomistic domain with and without filter

(b) Comparison of energies of atomistic and macro domain

Fig. 9. Evolution of energy in each domain.

of high-frequency component is largely mitigated. We may increase the size of the filter to further tune up the result.

To better exam the passage of information in the procedure, we plot the normalized energy of each region in macroscale time steps. Fig. 9(a) shows the evolution of elastic energy in the atomistic region with and without filter, respectively. When the macro time steps are between 2300 and 4300, the wave transits from atomistic and macro domain. Ideally, total energy in atomistic domain should be damped off after 4300 macro time steps, as shown in the energy profile with filter. However, when the filter is turned off, we only find a small amount of residual energy trapped in the fine scale zone, which is not physical. The filter is capable of removing more than 90% residual energy. The comparison of energy evolutions of both regions is shown in Fig. 9(b). When a solitary wave passing through the transition zone, energy in atomistic region decreases but increases in macro region. Before and after the transition, energy levels in both zones are all constant with normalized value of 0 and 1.

3.2. 2-D wave propagation

In the 2-D example problem, we choose the basal plane of the hexagonal close-packed (HCP) lattice as the model. The material is aluminum with an atomistic weight of 26.98 u same as the 1-D model. The lattice constant is $a_0 = 2.878$ Å. The same Morse potential is used for 2-D lattice. The shape of the multiscale elements in transition zone and material points in macro region is shown in Fig. 10. Each multiscale element includes 9 atoms. The distance from the center of each element to

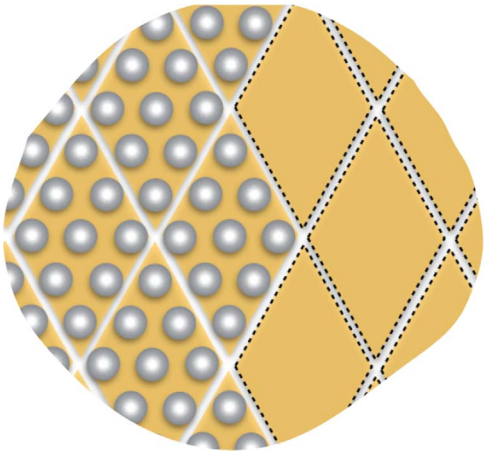

Fig. 10. Shape of the multiscale elements in transition zone and material points in macro region.

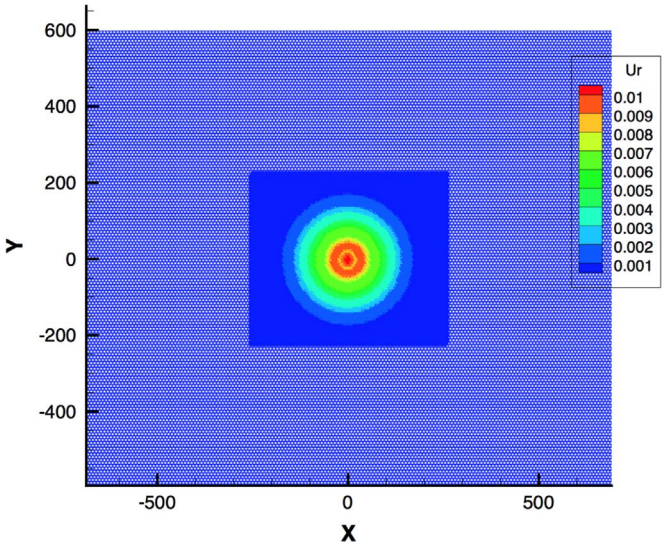

Fig. 11. Initial 2-D model setup: Inside is the atomistic region with rectangular shape, and a larger macro region surrounds the atomistic region. The initial wave profile is a Gaussian wave function with an amplitude magnitude of 0.01.

the nearest neighbor is $3a_0$. The 2D model has a rectangle shape as shown in Fig. 11. An atomistic region is located at the center with 150×150 atoms. The size is calculated as $150 \times 75\sqrt{3}\,a_0^2$ according to the lattice pattern. The transition zone surrounding the atomistic domain has a thickness of 5 multiscale element, in which a 2-element thickness is assigned as filter. Outside the atomistic region and the transition zone, a macro region with 160×160 material points or an area of the size $480 \times 240\sqrt{3}\,a_0^2$, except the fine scale center region, is constructed. Similar to the 1-D problem, the transient motion of a wave with initial shape of the Gaussian distribution in polar coordinate is examined,

$$u(r,\, t=0) = \begin{cases} A\exp\left(-\dfrac{r^2}{2\sigma^2}\right)\left(1 + b\cos\left(\dfrac{2\pi r}{H}\right)\right), & r \le L_c \\ 0, & r > L_c \end{cases} \tag{33}$$

where $A=0.01$, $\sigma=80$, $b=0.08$, and $H=\sigma/2$, in angstrom. The truncation distance is given as $L_c = 3\sigma$. Multiple-time-step integration algorithm is used in numerical integration of the simulation. Time integration step sizes for atomistic and macro regions are $\Delta t_a = 0.001$ and $\Delta t_m = 0.008$ in picosecond. Time integration step sizes for the transition elements are: $\Delta t_s = 0.001$, $\Delta t_\phi = 0.001$ and $\Delta t_r = 0.001$. Numbers of other sub-step size are tested before simulation, in order to achieve the optimal results.

Fig. 12 shows the history of the wave propagation from atomistic region into the macroscale region. Fig. 12(a) is the initial wave profile (in terms of color contour) as mentioned above. Fig. 12(b) is the snapshot when the whole wave is still inside the atomistic domain. Two separate rings are formed with higher amplitude of the inner (the second) ring and lower amplitude of the outer (the first) ring. Subsequently, the outer ring passes through the interface where the multiscale

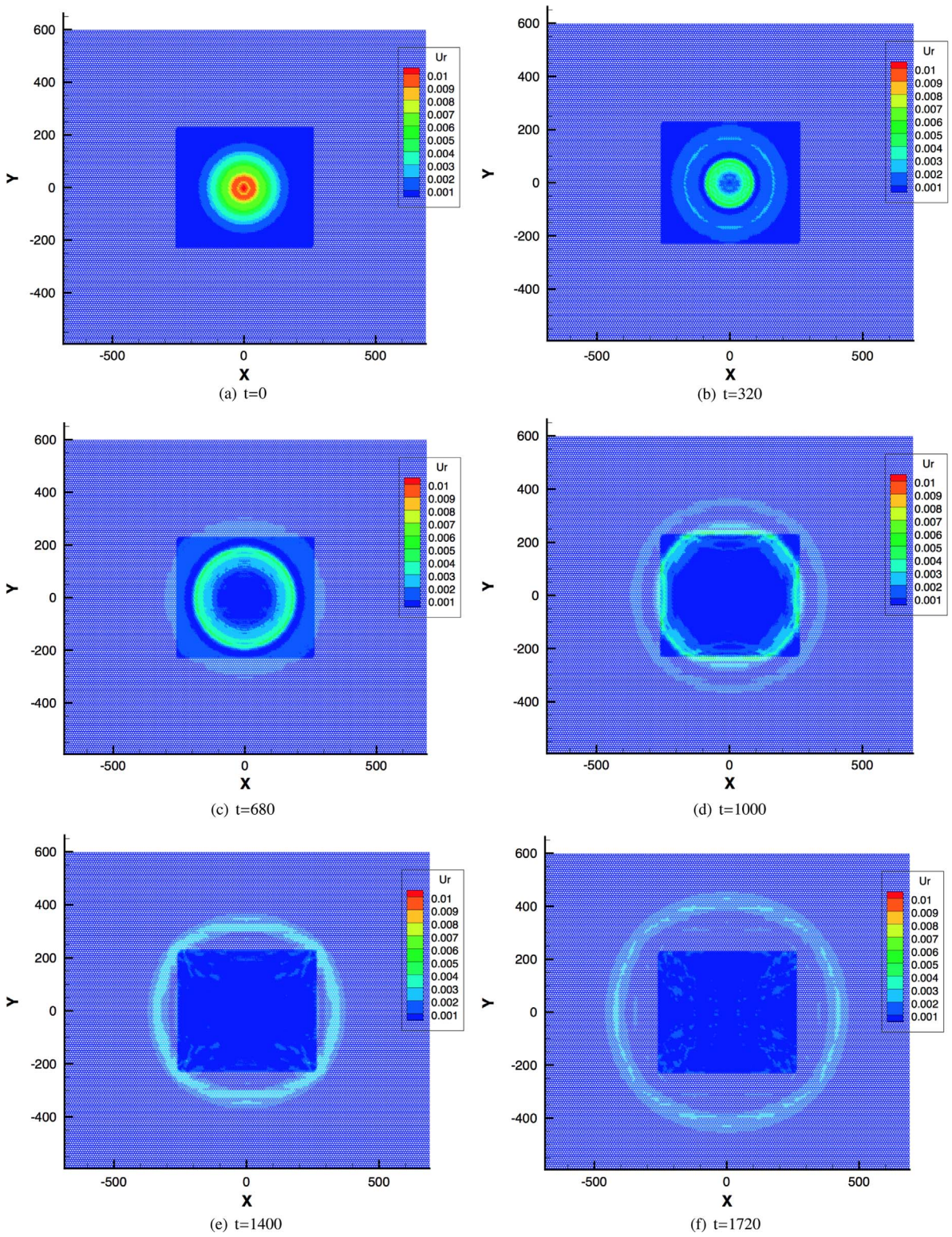

Fig. 12. History of wave propagation. The unit of time is in macroscale step size Δt_m.

elements are located to aid the transition. As shown in Fig. 12(c), the interface does not cause any visible mismatch or discontinuity, and the outer ring is smoothly distributed on both sides of the interface. Fig. 12(d) is the time instance when the inner ring is passing through the interface. We can see that even with the high magnitude and abrupt slope, the inner

ring still passes through without obvious interface scattering or diffraction. When the whole wave passes through the interface, as is shown in Fig. 12(e), small residual fluctuations are observed in the atomistic domain with sharp profiles at the corners near the interface. Note that the amplitude of the cylindrical wavefront will gradually die out when they propagate away as their radius expand, because of energy conservation. In Figs. 12(c), (d), (e) and (f), one can find that the first ring gradually disappeared first, and subsequently, the second ring is further propagating and also gradually disappeared in the macro region leaving a few hardly visible ripples inside as well as outside the fine scale region.

4. Summary and discussions

In this work, based on the multiscale micromorphic molecular dynamics theory, we proposed a multiscale computational model that couples Molecular Dynamics with Peridynamics. Instead of using prescribed multiscale interface conditions like many existing multiscale methods, we utilize the intrinsic multiscale characters of the molecular dynamics to construct a multiscale interphase zone that enables a seamless two-way message passing at multiscale boundary. By taking the advantage of multiscale structure in the interphase transition zone, we introduce an adaptive multiscale element to serve as a messenger on the interphase or transition zone that is responsible for exchanging information between different regions (scales) back and forth. Using MMMD formulation to construct the filter near the interface provides a simple way to smooth out high-frequency wave without sophisticated or ad hoc numerical treatment; thus the issue of reflection is greatly mitigated. By doing so, we have successfully realized both the bottom-up and the top-down message passings simultaneously, or concurrently, such that we can incorporate macroscale quantities such as traction and macroscale deformation into atomistic systems while extrapolating statistical Virial stress from microscale, which makes the proposed multiscale model capable of exchanging both atomistic and macro scale information through different regions in different scales.

The proposed multiscale model is based on fundamental physical principles rather than ad hoc numerical techniques, which renders the subsequent mathematical structure simple and straightforward. More importantly, it provides profound insights and understandings on multiscale mechanics and physics. A major numerical artifact in many existing multiscale methods is the assumption of uniform lattice deformation at the multiscale interface. This is tolerable in regular deformation such as wave propagation. However, it cannot capture inhomogeneous deformation such as phase transition or materials defect passing, which are often the cases on boundaries and interfaces. It has shown in this work that the proposed method can easily do that, because of the adaptive nature of the multiscale element, which can relax the internal motions of supercells, so that particles are free to move instead of being frozen in given positions and to seek the pattern or distribution in an optimal energy state.

As a multiscale method, we used the Cauchy–Born rule to calculate stress in macroscale peridynamics formulation such that we obtain the non-local macroscale constitutive relation through atomistic potentials, and it then avoids to use empirical or phenomenological constitutive relations to describe materials behaviors. Moreover, this work reports a particular coupling between molecular dynamics and peridynamics. To the best knowledge of the authors, it may be the first technical report on such coupling technique for two important particle methods. This may have a major consequence and development in the future.

To validate the proposed multiscale coupling method, we have implemented and analyzed test examples of 1-D and 2-D wave propagations. The numerical results in the 1-D example show that low-frequency wave can be smoothly transmitted through the interface, and the high-frequency wave can be filtered. The energy evolution is monitored and observed in regions of different scales, which provided solid evidence on the important role that the filter played. The 2D example has further demonstrated the efficiency of the proposed multiscale method by examining the detailed message passing process through the interface. The numerical results have clearly shown the advantage and the capability of the proposed method handling coupling of two different particle methods at ease.

Appendix. Derivation of multiscale micromorphic molecular dynamics

In this Appendix, for the sake of self-containedness, we provide the derivation of the governing equations of the Multiscale Micromorphic Molecular Dynamics, i.e. Eqs. (14)–(16).

The basic idea of the Multiscale Micromorphic Molecular Dynamics is to divide a finite molecular dynamics simulation region into finite number of supercells see Fig. 13. For the detailed discussions and physical background of such domain decomposition and associated multiscale decomposition, the readers are referred to Li and Tong (2015) and Tong and Li (2015a). For a representative supercell α, we have the following multiscale Lagrangian, i.e. Eq. (13),

$$\mathcal{L}_\alpha = K_\alpha - V_\alpha = \frac{1}{2}M_\alpha \dot{\mathbf{r}}_\alpha\cdot\dot{\mathbf{r}}_\alpha + \frac{1}{2}\dot{\boldsymbol{\phi}}_\alpha^T\dot{\boldsymbol{\phi}}_\alpha : \mathbf{J}_\alpha + \frac{1}{2}\mathbf{C}_\alpha : \sum_{i\in S_\alpha} m_i\dot{\mathbf{S}}_i\otimes\dot{\mathbf{S}}_i - \frac{1}{2}\sum_{i,j\in S_\alpha}\varphi(r_{ij}) - \sum_{i\in S_\alpha, j\notin S_\alpha}\varphi(r_{ij}) + S_\alpha^0\tilde{\mathbf{t}}_\alpha^0\cdot\mathbf{r}_\alpha, \tag{34}$$

which has three independent variables: $\mathbf{r}_\alpha$, $\boldsymbol{\phi}_\alpha$, and $\mathbf{S}_i$, and S_α is the atom number index set for the supercell α.

Note that there is very subtle point in this derivation. That is the Lagrangian defined in Eq. (34) is not addable, i.e. the total Lagrangian inside the whole solid, $\mathcal{L}_m$ is not equal to the sum of the Lagrangian in each supercell, i.e.

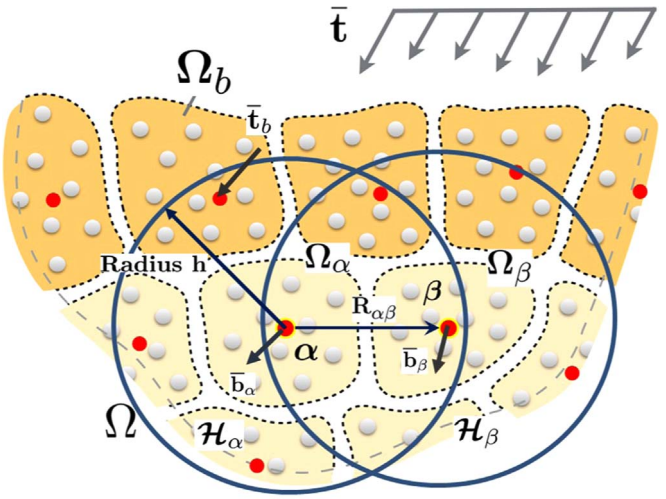

Fig. 13. Schematic illustration of supercell domain decomposition of MMMD.

$$\mathcal{L}_m \neq \sum_{\alpha\in S_N} \mathcal{L}_\alpha,$$

where S_α is the index set for all supercells. This is because $\mathcal{L}_\alpha$ has already contained all the interaction energy with adjacent supercells. More precisely speaking, there is no 1/2 factor in front the term $\sum_{i\in S_\alpha, j\notin S_\alpha}$.

It is noted that the total deformation tensor has a multiscale micromorphic decomposition,

$$\boldsymbol{\phi}_\alpha = \mathbf{F}_\alpha \cdot \boldsymbol{\chi}_\alpha,$$

where $\boldsymbol{\chi}_\alpha$ is the true independent kinematic variable, whose physical meaning is the microscale or mesoscale deformation tensor of the supercell; whereas $\mathbf{F}_\alpha$ is the macroscale deformation tensor, which can be determined by the spatial distribution of the supercell centers of mass i.e. $\mathbf{r}_\alpha$, and it may be determined by Eq. (7), making it consistent with the macroscale peridynamics.

Then the equations of motion for $\mathbf{r}_\alpha$, $\boldsymbol{\phi}_\alpha$ and $\mathbf{S}_i$ can be derived by deriving the Euler–Lagrange equations,

$$\frac{d}{dt}\left(\frac{\partial \mathcal{L}_\alpha}{\partial \dot{\mathbf{r}}_\alpha}\right) - \frac{\partial \mathcal{L}_\alpha}{\partial \mathbf{r}_\alpha} = 0, \tag{35}$$

$$\frac{d}{dt}\left(\frac{\partial \mathcal{L}_\alpha}{\partial \dot{\boldsymbol{\phi}}_\alpha}\right) - \frac{\partial \mathcal{L}_\alpha}{\partial \boldsymbol{\phi}_\alpha} = 0, \tag{36}$$

$$\frac{d}{dt}\left(\frac{\partial \mathcal{L}_\alpha}{\partial \dot{\mathbf{S}}_i}\right) - \frac{\partial \mathcal{L}_\alpha}{\partial \mathbf{S}_i} = 0, \tag{37}$$

where $\alpha \in S_N$, $i \in S_\alpha$, and S_N is the index set for all the supercells.

Before deriving the above equations, we observe the fact that the coarse scale deformation gradient depends on the relative displacements of all centers of mass, which is,

$$\mathbf{F}_\alpha = \mathbf{F}_\alpha(\{\mathbf{r}_\beta\}), \tag{38}$$

where $\{\mathbf{r}_\beta\}$ represent a set of all centers of mass. Then we have

$$\dot{\mathbf{F}}_\alpha = \mathbf{F}_\alpha(\{\mathbf{r}_\beta\}, \{\dot{\mathbf{r}}_\beta\}). \tag{39}$$

From Eq. (38), we also have,

$$\dot{\mathbf{F}}_\alpha = \sum_\beta \frac{\partial \mathbf{F}_\alpha}{\partial \mathbf{r}_\beta}\dot{\mathbf{r}}_\beta, \tag{40}$$

therefore,

$$\frac{\partial \dot{\mathbf{F}}_\alpha}{\partial \dot{\mathbf{r}}_\alpha} = \frac{\partial \mathbf{F}_\alpha}{\partial \mathbf{r}_\alpha}. \tag{41}$$

From Eq. (39), we can derive,

$$\ddot{\mathbf{F}}_\alpha = \sum_\beta \left[\frac{\partial \dot{\mathbf{F}}_\alpha}{\partial \mathbf{r}_\beta} \dot{\mathbf{r}}_\beta + \frac{\partial \dot{\mathbf{F}}_\alpha}{\partial \dot{\mathbf{r}}_\beta} \ddot{\mathbf{r}}_\beta \right]. \tag{42}$$

On the other hand, from Eq. (40), the relation is,

$$\ddot{\mathbf{F}}_\alpha = \sum_\beta \left[\frac{d}{dt}\left(\frac{\partial \mathbf{F}_\alpha}{\partial \mathbf{r}_\beta} \right) \dot{\mathbf{r}}_\beta + \frac{\partial \mathbf{F}_\alpha}{\partial \mathbf{r}_\beta} \ddot{\mathbf{r}}_\beta \right]. \tag{43}$$

Comparing Eqs. (43) and (44), and using relation (41), we obtain,

$$\frac{\partial \dot{\mathbf{F}}_\alpha}{\partial \mathbf{r}_\alpha} = \frac{d}{dt}\left(\frac{\partial \mathbf{F}_\alpha}{\partial \mathbf{r}_\beta} \right). \tag{44}$$

Recall that the total deformation $\boldsymbol{\phi}_\alpha = \mathbf{F}_\alpha \cdot \boldsymbol{\chi}_\alpha$, then the time derivative is,

$$\dot{\boldsymbol{\phi}}_\alpha = \dot{\mathbf{F}}_\alpha \cdot \boldsymbol{\chi}_\alpha + \mathbf{F}_\alpha \cdot \dot{\boldsymbol{\chi}}_\alpha. \tag{45}$$

By knowing the fact that $\boldsymbol{\chi}_\alpha$ is an independent variable, and using relations (42) and (45), we have

$$\frac{\partial \dot{\boldsymbol{\phi}}_\alpha}{\partial \dot{\mathbf{r}}_\alpha} = \frac{\partial \dot{\mathbf{F}}_\alpha}{\partial \dot{\mathbf{r}}_\alpha} \boldsymbol{\chi}_\alpha = \frac{\partial \mathbf{F}_\alpha}{\partial \mathbf{r}_\alpha} \boldsymbol{\chi}_\alpha = \frac{\partial \boldsymbol{\phi}_\alpha}{\partial \mathbf{r}_\alpha}, \tag{46}$$

and

$$\frac{\partial \dot{\boldsymbol{\phi}}_\alpha}{\partial \mathbf{r}_\alpha} = \frac{\partial \dot{\mathbf{F}}_\alpha}{\partial \mathbf{r}_\alpha} \boldsymbol{\chi}_\alpha + \frac{\partial \mathbf{F}_\alpha}{\partial \mathbf{r}_\alpha} \dot{\boldsymbol{\chi}}_\alpha = \frac{d}{dt}\left(\frac{\partial \mathbf{F}_\alpha}{\partial \mathbf{r}_\beta} \right) \boldsymbol{\chi}_\alpha + \frac{\partial \mathbf{F}_\alpha}{\partial \mathbf{r}_\alpha} \dot{\boldsymbol{\chi}}_\alpha = \frac{d}{dt}\left(\frac{\partial \boldsymbol{\phi}_\alpha}{\partial \mathbf{r}_\alpha} \right) = \frac{d}{dt}\left(\frac{\partial \dot{\boldsymbol{\phi}}_\alpha}{\partial \dot{\mathbf{r}}_\alpha} \right). \tag{47}$$

First, we can calculate the dynamic equations for $\mathbf{r}_\alpha$,

$$\frac{d}{dt}\left(\frac{\partial \mathcal{L}_\alpha}{\partial \dot{\mathbf{r}}_\alpha} \right) = \frac{d}{dt}\left(\frac{\partial \mathcal{L}_\alpha}{\partial \dot{\mathbf{r}}_\alpha} + \frac{\partial \mathcal{L}_\alpha}{\partial \dot{\boldsymbol{\phi}}_\alpha} \cdot \frac{\partial \dot{\boldsymbol{\phi}}_\alpha}{\partial \dot{\mathbf{r}}_\alpha} \right) = M_\alpha \ddot{\mathbf{r}}_\alpha + \frac{d}{dt}\left(\frac{\partial \mathcal{L}_\alpha}{\partial \dot{\boldsymbol{\phi}}_\alpha} \right) \cdot \frac{\partial \dot{\boldsymbol{\phi}}_\alpha}{\partial \dot{\mathbf{r}}_\alpha} + \frac{\partial \mathcal{L}_\alpha}{\partial \dot{\boldsymbol{\phi}}_\alpha} \cdot \frac{d}{dt}\left(\frac{\partial \dot{\boldsymbol{\phi}}_\alpha}{\partial \dot{\mathbf{r}}_\alpha} \right), \tag{48}$$

and

$$\frac{\partial \mathcal{L}_\alpha}{\partial \mathbf{r}_\alpha} = \frac{\partial \mathcal{L}_\alpha}{\partial \mathbf{r}_\alpha} + \frac{\partial \mathcal{L}_\alpha}{\partial \boldsymbol{\phi}_\alpha} \cdot \frac{\partial \boldsymbol{\phi}_\alpha}{\partial \mathbf{r}_\alpha} + \frac{\partial \mathcal{L}_\alpha}{\partial \dot{\boldsymbol{\phi}}_\alpha} \cdot \frac{\partial \dot{\boldsymbol{\phi}}_\alpha}{\partial \mathbf{r}_\alpha} = S_\alpha^0 \bar{\mathbf{t}}_\alpha + \frac{\partial \mathcal{L}_\alpha}{\partial \boldsymbol{\phi}_\alpha} \cdot \frac{\partial \boldsymbol{\phi}_\alpha}{\partial \mathbf{r}_\alpha} + \frac{\partial \mathcal{L}_\alpha}{\partial \dot{\boldsymbol{\phi}}_\alpha} \cdot \frac{\partial \dot{\boldsymbol{\phi}}_\alpha}{\partial \mathbf{r}_\alpha}. \tag{49}$$

Considering the relations in Eqs. (47), (48) and (36), last two terms in Eqs. (49) and (50) are canceled when they are substituted into Eq. (35), we have finally derived Eq. (10), i.e.

$$M_\alpha \ddot{\mathbf{r}}_\alpha = \sum_{i \in S_\alpha, j \notin S_\alpha} \mathbf{f}_{ij} + S_\alpha^0 \bar{\mathbf{t}}_\alpha, \tag{50}$$

where $\mathbf{f}_{ij} = \varphi'(r_{ij}) \mathbf{r}_{ij} / |\mathbf{r}_{ij}|$.

Moreover, it is straightforward to show that

$$\frac{d}{dt}\left(\frac{\partial \mathcal{L}_\alpha}{\partial \boldsymbol{\phi}_\alpha} \right) = \frac{d}{dt}\left(\dot{\boldsymbol{\phi}}_\alpha \cdot \mathbf{J} \right) = \ddot{\boldsymbol{\phi}}_\alpha \cdot \mathbf{J}_\alpha, \tag{51}$$

and

$$\frac{\partial \mathcal{L}_\alpha}{\partial \boldsymbol{\phi}_\alpha} = \boldsymbol{\phi}_\alpha \cdot \sum_{i \in S_\alpha} m_i \dot{\mathbf{s}}_i \otimes \dot{\mathbf{s}}_i - \frac{1}{2} \sum_{i,j \in S_\alpha} \varphi'(r_{ij}) \frac{\mathbf{r}_{ij}}{r_{ij}} \cdot \frac{\partial \mathbf{r}_{ij}}{\partial \boldsymbol{\phi}_\alpha} - \sum_{i,j \in S_\alpha, j \notin S_\alpha} \varphi'(r_{ij}) \frac{\mathbf{r}_{ij}}{r_{ij}} \cdot \frac{\partial \mathbf{r}_{ij}}{\partial \boldsymbol{\phi}_\alpha}. \tag{52}$$

By considering the fact that

$$\frac{\partial \mathbf{r}_{ij}}{\partial \boldsymbol{\phi}_\alpha} = \begin{cases} \mathbf{I} \otimes \mathbf{S}_{ij}, & i, j \in S_\alpha \\ -\mathbf{I} \otimes \mathbf{S}_{ij}, & i, j \notin S_\alpha \end{cases},$$

we have

$$\frac{\partial \mathcal{L}_\alpha}{\partial \boldsymbol{\phi}_\alpha} = \boldsymbol{\phi}_\alpha \cdot \sum_{i \in S_\alpha} m_i \dot{\mathbf{S}}_i \otimes \dot{\mathbf{s}}_i - \frac{1}{2} \sum_{i,j \in S_\alpha} \mathbf{f}_{ij} \otimes \mathbf{S}_{ij} + \sum_{i,j \in S_\alpha, j \notin S_\alpha} \mathbf{f}_{ij} \otimes \mathbf{S}_{ij}. \tag{54}$$

The dynamics equation for $\boldsymbol{\phi}_\alpha$ can be written as,

$$\ddot{\boldsymbol{\phi}}_\alpha \cdot \mathbf{J} = (\mathcal{P}_\alpha^{ext} - \mathcal{P}_\alpha^{int})\Omega_\alpha^0, \tag{55}$$

where

$$\mathcal{P}_\alpha^{int} = \frac{1}{\Omega_\alpha^0}\left(\frac{1}{2}\sum_{i,j\in S_\alpha}\mathbf{f}_{ij}\otimes\mathbf{S}_{ij} - \boldsymbol{\phi}_\alpha\cdot\sum_{i\in S_\alpha} m_i\dot{\mathbf{S}}_i\otimes\dot{\mathbf{S}}_i\right), \tag{56}$$

$$\mathcal{P}_\alpha^{ext} = \frac{1}{\Omega_\alpha^0}\sum_{i\in S_\alpha, j\notin S_\alpha}\mathbf{f}_{ij}\otimes\mathbf{S}_{ij}. \tag{57}$$

which are exactly the same as Eqs. (15), (17) and (18).

Last, we consider the dynamic equations for $\mathbf{S}_i$,

$$\frac{d}{dt}\left(\frac{\partial\mathcal{L}_\alpha}{\partial\dot{\mathbf{S}}_i}\right) = \frac{d}{dt}(m_i\mathbf{C}_\alpha\cdot\dot{\mathbf{S}}) = m_i\dot{\mathbf{C}}_\alpha\cdot\dot{\mathbf{S}}_i + m_i\mathbf{C}_\alpha\cdot\ddot{\mathbf{S}}_i \tag{58}$$

and

$$\frac{\partial\mathcal{L}_\alpha}{\partial\mathbf{S}_i} = -\sum_{i,j\in S_\alpha}\varphi'(r_{ij})\frac{\mathbf{r}_{ij}}{r_{ij}}\frac{\partial\mathbf{r}_{ij}}{\partial\mathbf{S}_i} - \sum_{i\in\alpha, j\notin S_\alpha}\varphi'(r_{ij})\frac{\mathbf{r}_{ij}}{r_{ij}}\frac{\partial\mathbf{r}_{ij}}{\partial\mathbf{S}_i} = \sum_j \mathbf{f}_{ij}\otimes\boldsymbol{\phi}_\alpha, \tag{59}$$

which lead to the microscale dynamic equation,

$$m_i\mathbf{C}_\alpha\cdot\ddot{\mathbf{s}} = \sum_j \mathbf{f}_{ij}\cdot\boldsymbol{\phi}_\alpha - m_i\dot{\mathbf{C}}_\alpha\cdot\dot{\mathbf{S}}_i. \tag{60}$$

Eq. (60) is exactly Eq. (16). Note that in Eqs. (59) and (60) the summation $\sum_j$ denotes the sum of all other atom j in the whole domain of the solid that is under study, which are not just those atoms inside the supercell α.

References

Abraham, F.F., Broughton, J.Q., Bernstein, N., Kaxiras, E., 1998. Spanning the continuum to quantum length scales in a dynamic simulation of brittle fracture. Europhys. Lett. 44 (6), 783–787.

Askari, E., Silling, S.A., 2005. A meshfree method based on the peridynamic model of solid mechanics. Comput. Struct. 83 (17), 1526–1535.

Broughton, J.Q., Abraham, F.F., Bernstein, N., Kaxiras, E., 1999. Concurrent coupling of length scales: methodology and application. Phys. Rev. B 60 (4), 2391–2403.

Car, R., Parrinello, M., 1985. Unified approach for molecular dynamics and density-functional theory. Phys. Rev. Lett. 55 (22), 2471.

Chen, Y., Lee, J., 2005. Atomistic formulation of a multiscale field theory for nano/micro solids. Philos. Mag. 85 (33), 4095–4126.

Gear, C.W., 1971. The automatic integration of ordinary differential equations. Commun. ACM 14 (3), 176–179.

Hohenberg, P., Kohn, W., 1964. Inhomogeneous electron gas. Phys. Rev. 136 (3B), B864.

Hou, C., Xu, J., Wang, P., Huang, W., Wang, X., Ge, W., He, X., Guo, L., Li, J., 2012. Petascale molecular dynamics simulation of crystalline silicon on Tianhe-1A. Int. J. High Perform. Comput. Appl. 1094342012456047 (August), 1–11.

Knap, J., Ortiz, M., 2001. An analysis of the quasicontinuum method. J. Mech. Phys. Solids 49 (9), 1899–1923.

Kohn, W., Sham, L.J., 1965. Self-consistent equations including exchange and correlation effects. Phys. Rev. 140 (4A), A1133.

Lee, E.H., 1969. Elastic–plastic deformation at finite strains. J. Appl. Mech. 36, 1–6.

Li, S., Liu, W.K., 2002. Meshfree and particle methods and their applications. Appl. Mech. Rev. 55 (1), 1–34.

Li, S., Tong, Q., 2015. A concurrent multiscale micromorphic molecular dynamics. J. Appl. Phys. 117, 154303.

Li, S., Urata, S., 2016. An atomistic-to-continuum molecular dynamics: theory, algorithm, and applications. Comput. Methods Appl. Mech. Eng. 306, 452–478.

Li, S., Liu, X., Agrawal, A., To, A.C., 2006. Perfectly matched multiscale simulations for discrete lattice systems: extension to multiple dimensions. Phys. Rev. B 74 (4), 045418.

Li, S., Ren, B., Minaki, H., 2014. Multiscale crystal defect dynamics: a dual-lattice process zone model. Philos. Mag. 94, 1414–1450.

Liu, W.K., Jun, S., Li, S., Adee, J., Belytschko, T., 1995. Reproducing kernel particle methods for structural dynamics. Int. J. Numer. Methods Eng. 38 (10), 1655–1679.

Liu, W.K., Park, H.S., Qian, D., Karpov, E.G., Kadowaki, H., Wagner, G.J., 2006. Bridging scale methods for nanomechanics and materials. Comput. Methods Appl. Mech. Eng. 195 (13), 1407–1421.

Park, H.S., Karpov, E.G., Liu, W.K., Klein, P.A., 2005a. The bridging scale for two-dimensional atomistic/continuum coupling. Philos. Mag. 85 (1), 79–113.

Park, H.S., Karpov, E.G., Klein, P.A., Liu, W.K., 2005b. Three-dimensional bridging scale analysis of dynamic fracture. J. Comput. Phys. 207 (2), 588–609.

Parrinello, M., Rahman, A., 1981. Polymorphic transitions in single crystals: a new molecular dynamics method. J. Appl. Phys. 12, 7182–7190.

Podio-Guidugli, P., 2010. On (Andersen)–Parrinello–Rahman molecular dynamics, the related metadynamics, and the use of the Cauchy–Born rule. J. Elast. 100, 145–153.

Shenoy, V.B., Miller, R., Tadmor, E.B., Phillips, R., Ortiz, M., 1998. Quasicontinuum models of interfacial structure and deformation. Phys. Rev. Lett. 80 (4), 742–745.

Shenoy, V.B., Miller, R., Tadmor, E.b., Rodney, D., Phillips, R., Ortiz, M., 1999. An adaptive finite element approach to atomic-scale mechanics—the quasicontinuum method. J. Mech. Phys. Solids 47 (3), 611–642.

Shilkrot, L.E., Miller, R.E., Curtin, W.A., 2002. Coupled atomistic and discrete dislocation plasticity. Phys. Rev. Lett. 89 (2), 025501.

Shilkrot, L.E., Miller, R.E., Curtin, W.A., 2004. Multiscale plasticity modeling: coupled atomistics and discrete dislocation mechanics. J. Mech. Phys. Solids 52 (4), 755–787.

Silling, S.A., 2000. Reformulation of elasticity theory for discontinuities and long-range forces. J. Mech. Phys. Solids 48 (1), 175–209.

Silling, S.A., Lehoucq, R.B., 2010. Peridynamic theory of solid mechanics. Adv. Appl. Mech. 44 (1), 73–166.

Silling, S.A., Epton, M., Weckner, O., Xu, J., Askari, E., 2007. Peridynamic states and constitutive modeling. J. Elast. 88 (2), 151–184.

Tadmor, E.B., Ortiz, M., Phillips, R., 1996. Quasicontinuum analysis of defects in solids. Philos. Mag. A 73 (6), 1529–1563.
To, A.C., Li, S., 2005. Perfectly matched multiscale simulations. Phys. Rev. B 72 (3), 035414.
Tong, Q., Li, S., 2015a. From molecular systems to continuum solids: a multiscale structure and dynamics. J. Chem. Phys. 143 (6), 064101.
Tong, Q., Li, S., 2015b. A multiscale molecular dynamics allowing macroscale mechanical loads. Europhys. Lett. 110 (6), 60005.
Ulz, M.H., 2015. Coupling the finite element method and molecular dynamics in the framework of the heterogeneous multiscale method for quasi-static isothermal problems. J. Mech. Phys. Solids 74, 1–18.
Verlet, L., 1967. Computer "experiments" on classical fluids. I. Thermodynamical properties of Lennard–Jones molecules. Phys. Rev. 159 (1), 98.
Wagner, G.J., Liu, W.K., 2003. Coupling of atomistic and continuum simulations using a bridging scale decomposition. J. Comput. Phys. 190 (1), 249–274.
Xiong, L., Tucker, G., McDowell, D.L., Chen, Y., 2011. Coarse-grained atomistic simulation of dislocations. J. Mech. Phys. Solids 59 (2), 160–177.